3D Microstructural characterization of a solid oxide fuel cell anode reconstructed by focused ion beam tomography

N. Vivet, S. Chupin, E. Estrade, T. Piquero, P.L. Pommier, D. Rochais, E. Bruneton*

*CEA, Le Ripault, BP 16, 37260 Monts, France*

ABSTRACT

The three-dimensional microstructure of an SOFC anode has been characterized using a focused ion beam-scanning electron microscope. The sample preparation and the experimental milling and imaging parameters have been optimized in order to obtain a high-quality 3D reconstruction. Volume fractions and the volumetric connectivity of the individual phases, specific surface and interface areas and the three-phase boundary length have been estimated. Effective thermal, electronic and ionic conductivities of the sample as well as the tortuosity of the solid phases have been evaluated by solving the diffusive transport equation with an implicit 3D finite difference method.

© 2011 Elsevier B.V. All rights reserved.

1. Introduction

The solid oxide fuel cell (SOFC) technology is one of the most promising energy conversion systems due to its high efficiency and fuel flexibility [1]. The materials involved in the constitution of such fuel cells have become increasingly sophisticated, both in composition and microstructure. One of the most common anode materials for SOFCs is a porous Ni–YSZ cermet. The anode is the place where the oxidation of the fuel gas occurs according to the reaction:

$$H_2 + O^{2-} \rightarrow H_2O + 2e^-$$
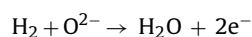
The most important requirements for the anode are:

(1) *catalytic activity*: the anode must have a high catalytic activity for the oxidation of the fuel gas: the greater the number of reaction sites the greater the potential for chemical reactions;
(2) *stability*: the anode must be chemically, morphologically, and dimensionally stable at the required operating temperature in the fuel gas environment; it must also be resistant towards contaminants;
(3) *conductivity*: the greatest electrical conductivity under a large variety of operating conditions is desired to minimize ohmic losses, and a high ionic (O^{2-}) conductivity is also expected in order to promote the reaction of the fuel with oxide ions;

(4) *compatibility*: the anode must be chemically, thermally, and mechanically compatible with the other cell components during fabrication as well as under operation;
(5) *porosity*: the porosity of the anode must be adapted to optimize mass transport.

For most of these conditions, some experimental studies have been performed to estimate the corresponding parameters: volume fraction, phase connectivity, specific surface area, three-phase boundary length (TPB_L), tortuosity, as well as thermal, electrical and ionic conductivities. These parameters can only be described three-dimensionally and thus cannot be estimated using current methods of microstructural analysis, like for example scanning electron microscopy (SEM) which only provides two-dimensional singularities of the microstructure.

Recently, 3D reconstructions of SOFC electrodes (both anode and cathode with characteristic particle sizes in the range of 100–500 nm) have been performed by X-ray computed tomography (XCT) [2–5] and primarily by focused ion beam-scanning electron microscopy (FIB-SEM) [6–22]. The FIB tomography principle consists in ablating a structure physically by FIB slicing (Ga^+ ions) followed by a digital reconstruction based on SEM images collected after each ablation step. The process can be carried out manually or automatically. The obtained images are then aligned and superimposed in order to generate the volume. A few hundred images are recorded with an inter-slice distance of about 30–100 nm (volume dimension typically close to $10 \times 10 \times 10 \, \mu m^3$). The voxel dimensions and the size of the analyzed volume must be optimized according

---

* Corresponding author. Tel.: +33 247344193; fax: +33 247345174.
E-mail address: eric.bruneton@cea.fr (E. Bruneton).

Table 1
Characteristic data of the starting powders and ink.

Components	Suppliers	Particle size, d_{50} (µm)[a]	Surface area (m² g⁻¹)[a]	Viscosity (Pa s @ 10 s⁻¹)[b]
TZ-8YS powder	Tosoh	0.55	6.20	
NiO powder	JT Baker	0.9	3.30	–
Ink medium	Nextech materials	–	–	0.1

[a] Data measured from Cilas granulometer.
[b] Information from the supplier.

to the particle size and heterogeneity of the studied sample [23].

As described below, the obtained 3D microstructure can be either analyzed to extract some 3D physical parameters or directly implemented into numerical models, in order to for example calculate the transport properties (of gas, heat, ions and electrons). On the one hand, the volume data can be used to estimate features like volume fraction, phase connectivity, interfacial areas, TPB_L and tortuosity. The microstructure is therefore described by some geometrical 3D parameters. These parameters are then included into analytic relations originating from simple models or experimental measurements to evaluate the electrochemical performance of the corresponding sample. For instance, the Tanner–Fung–Virkar composite electrode model [24] has been employed to predict the polarization resistance of SOFC anodes and cathodes [7,11]. Electrochemical impedance measurements on SOFC cathodes have also been correlated to 3D analysis to establish an analytical relation between the polarization resistance and the TPB_L [14,15].

On the other hand, the data can also be used as input for SOFC transport models to assess the electrode performance. For instance, the anodic overpotential has been calculated by coupling the mass and charge transfer and the electrochemical reaction using the Lattice Boltzmann method [18]. These two approaches have been applied to electrodes with different YSZ/Ni ratios [11,12,14] or subjected to aging under a controlled environment including temperature, fuel composition or humidity [20,21].

The present study employed the optimization approach to obtain a high-quality 3D reconstruction of an Ni–YSZ anode using FIB-SEM. Then, from these 3D data, various microstructural parameters (volume fraction, phase connectivity), and interfacial parameters (surface area and TPB_L) were quantified. Moreover, by solving the diffusive transport equation on the analyzed volume, the effective thermal, electrical and ionic conductivities of the sample and the tortuosity of the solid phases could be estimated.

2. Experimental

2.1. Preparation of the anodic cermet

The deposition of the analyzed NiO–8YSZ anode (a three-layer coating on the electrolyte substrate) was performed by screen-printing onto circular 8 mol.% yttria doped-zirconia (8YSZ) supports using ink with an optimized composition and viscosity. NiO from J.T. Baker (USA) and 8YSZ from Tosoh (Japan) were used as the raw materials to prepare the NiO–8YSZ cermet at varying Ni volume ratios. Table 1 gives the particle size, surface area and ink viscosity.

First of all, in order to prepare a composite powder with an NiO ratio of 56 wt.% (corresponding to 40 vol.% Ni), the starting powders were weighed and ball-milled in ethanol during 18 h. Next, the solvent was evaporated in an atex oven during 24 h at 90 °C. After cooling, and to prevent agglomerates from forming, a 200-µm screening led to an NiO–8YSZ composite powder with the desired NiO ratio.

The anode ink was obtained by mixing the NiO–8YSZ powder (65.5 wt.%) with alpha-terpiniol (4.9 wt.%) and Nextech ink (27.8 wt.%) as the solvent and medium, respectively, and alkyl ether phosphate acid was employed as the dispersant (1.8 wt.%). After mixing and grinding the anode ink for 15 min, it was screen-printed onto circular zirconia supports through PET1000 screens. The first layer of the anode ink was dried in an oven for 20 min at 100 °C before a second layer of the same anode composition was screen-printed onto the first. The deposition of the third layer was processed in the same way. The electrodes were fired at 1300 °C during 3 h. The reduction treatment was performed at 800 °C for 4 h using a 2 °C min⁻¹ ramp rate in Ar–H₂ (2 vol.%, 0.5 l min⁻¹). By assuming a complete reduction of the NiO in Ni, the 8YSZ/Ni volume ratio was expected to be 60/40 after the reduction treatment.

2.2. FIB procedure

The image set was collected with a FEI dual-beam Strata 400-S FIB system. The procedure to obtain the 3D data from the initial sample is schematically presented in Fig. 1 and described as follows.

2.2.1. Sample preparation before FIB experiment

In order to easily distinguish the pores during SEM observation and to avoid mistakes due to the depth of field in the SEM images, the sample was infiltrated with an epoxy resin under vacuum (EPOFIX, Struers). Subsequently, it was polished up to a 0.5 µm finishing and cut to obtain a typical thinness of 500 µm. This was done to limit sample drift during FIB operation. Finally the sample was glued onto an aluminum stub, and a conducting gold layer (∼100 nm) was deposited by sputtering.

2.2.2. Preparation of the region of interest (ROI)

The sample was then mounted in the microscope chamber and adjusted to eucentric height so that the exposed surface could be imaged directly in SEM mode without repositioning. To this end, as illustrated in Fig. 2, the sample surface was perpendicular to the ion gun and at an angle of 52° with respect to the electron gun.

Prior to the FIB slicing process, a representative cross-sectional area of the sample was located by electron imaging and coated with a Pt protective layer of 2–3 µm (Fig. 2) using an in situ metallorganic ion source. This was done in order to protect the sample from accidental ion milling and erosion during ion-beam imaging and also to smooth the surface topography. Above all it was necessary to avoid, or at least strongly reduce a common artifact known as "water-falling" or the "curtaining" effect, seen as an example on the cross section in Fig. 3(a) since it occluded the entire image. A Pt deposition associated with sample infiltration and surface polishing have thus been realized

FIB was used to mill wide and deep trenches around the ROI with a maximal aperture current of 21 nA, giving rise to a "U-shaped trench" [12]. A relatively high dimension-free space around the ROI was essential to prevent the re-deposition of the sputtered material during the sectional milling process. If the space around the ROI was too small, images with high concentrations of artifact features or uneven brightness were obtained (Fig. 3(b)).

2.2.3. Milling and imaging process

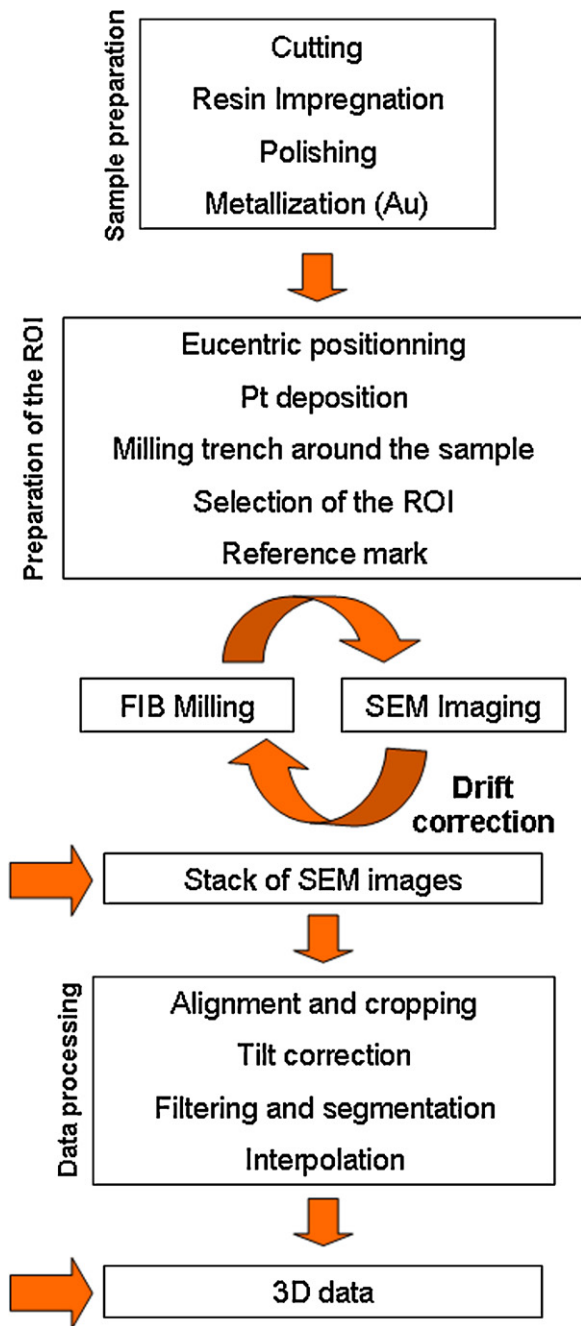In order to determine the depth removed in the z direction (see Fig. 2) between two consecutive sections (interslice: Δz), the rel-

Fig. 1. Schematic representation of the experimental method used to obtain the 3D reconstruction of the SOFC anode from FIB tomography.

Fig. 2. SEM image of the sample before the "milling and imaging" procedure. The stage tilt was kept the constant angle of 52° from the electron beam while the sample surface (*xz* plane) was perpendicular to the ion beam (*y* direction). The region of interest (ROI) is displayed in the orange rectangle. The sample was sliced in the *z* direction. The small rectangle on the Pt deposition (reference mark) was used to measure the interslice (Δz) and correct for drifting effects.

The SEM and FIB operating conditions for the sequential ion milling and electron imaging were optimized. The FIB milling was performed with an ion-beam current of 460 pA at 30 kV. For SEM imaging, a magnification of 12 kX and a Through the Lens Detector (TLD) operating in BSE mode at a low scan rate were employed. As the difference between the backscatter coefficients of Ni and 8YSZ were at a maximum for an accelerating voltage smaller than 1 kV [25], a 0.5-kV accelerating voltage provided an optimal contrast between Ni (bright), 8YSZ (grey) and the pores (dark) (Fig. 4(a)). Moreover, this low voltage rendered possible the collection of only backscattered electrons (BSE) emitted very close to the imaged surface.

Indeed, if the interaction region between the electron beam and the material is larger than the interslice value, the 3D imaging will not be correct. Monte Carlo calculations were performed with the CASINO software [26] on each constituent of the studied electrode: Ni, 8YSZ and resin (density: 8.9, 5.9 and 1.1 g cm^{-3} respectively) and displayed that for a 0.5-kV accelerating voltage, BSEs arose from a maximum depth of 6 nm, which was much smaller than the measured interslice value equal to 100 nm. In this case, 115 images were recorded using a manual procedure along the sample thickness (Fig. 4(a)). Including the in situ sample preparation and sectioning, the total processing time was approximately 18 h.

2.2.4. Data processing

Data processing includes the following steps: (i) alignment of the consecutives slices, (ii) correction of the dimensions taking into account the tilt of the electron beam, (iii) thresholding of the grey levels and labeling of phases, (iv) resampling of the data to obtain cubic voxels and (v) 3D image generation. Most of the processing steps were performed using the AVIZO 6.2 software [27]. Details of each step are given below.

The still remaining drift components of the electron beam in the *x* and *y* directions were corrected by applying least square fitting algorithms to achieve a correct alignment of the images. Finally, the resulting volume was cropped to keep only the ROI common to all slices. The absolute dimensions in the *x* direction were obtained from a calibrated SEM magnification. Because of oblique SEM imaging at an angle of 52°, distances in the *y* direction were corrected for

ative recession of the depth-profiled surface was measured and compared to the original cross-section based on a reference mark (rectangle) on the upper part of the Pt layer. Since the "milling and imaging" procedure was very time-consuming, uncorrected drift of electron beam, stage and sample could greatly affect the interslice real value. For this reason a correction procedure was utilized [23]. Drift values in the *x* and *z* directions were measured and corrected after each slicing and imaging loop. For this purpose, an image containing the reference mark (rectangle in Fig. 2) was acquired using the ion-induced secondary electron detector (CDEM: continuous dynode electron multiplier) located perpendicularly to the sample surface. Before recording an image used for the reconstruction, a CDEM image was registered and the ion beam was eventually deflected to allow perfect matching between the actual and original positions of the milled rectangle.
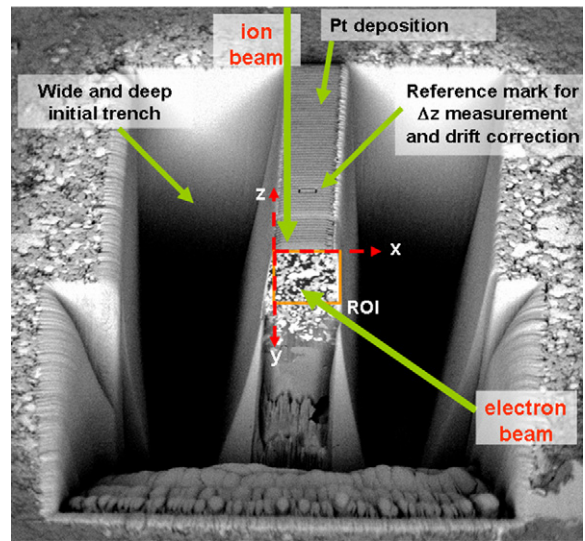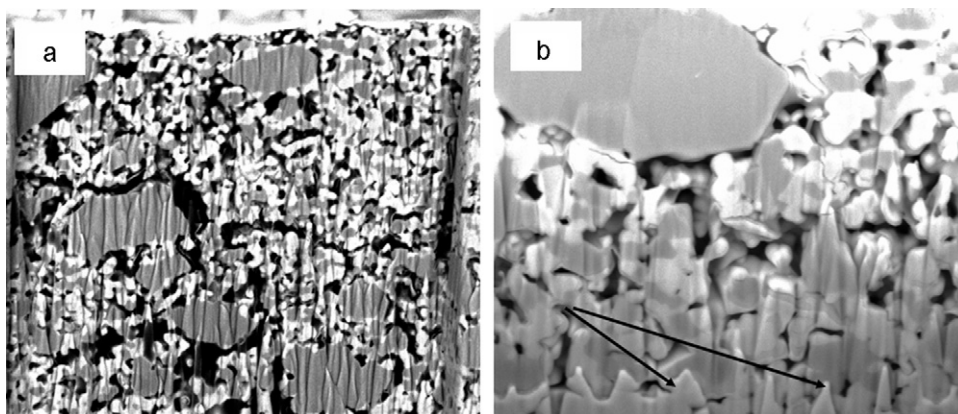
Fig. 3. SEM images of a Ni–8YSZ anode illustrating some common FIB artifacts: (a) "curtaining" effect due to a too small (<1 μm) Pt thickness, (b) deposition of the sputtered material (arrows) and shadowing effect (uneven brightness from the top to the bottom of the image) occurring when trenches around the ROI are not sufficiently deep and wide.

projection effects using $y_{real} = y_{SEM\_image}/\sin(52°)$. In certain cases, a slight tilting occurred because of imperfect straight milling in the XZ plane (see Fig. 2); however, since the 460 pA milling current was small, this effect was neglected. The 3D image dimensions were finally $8.66 \times 9.79 \times 11.41 \ \mu m^3$ (volume = 967.36 μm^3).

Even though a good and reproducible contrast between the three phases could be obtained, the boundaries between them were generally not perfectly sharp lines, but rather gradual transition zones a few voxels wide. Consequently, a median filter and a delineating operation were applied to the entire stack of images to obtain a good separation between each phase. Segmentation of the data (assigning a phase to a voxel) was then realized by grey level-based thresholding (Fig. 4(b)).

The initial dimension of voxels was $10.4 \times 13.2 \times 100 \ nm^3$. However, the dataset was resampled to obtain approximately one billion $10 \times 10 \times 10 \ nm^3$ cubic voxels using a cubic interpolation method. This was due to the fact that the following analysis method (TPB$_L$ and tortuosity measurements) required cubic voxels. The resampling step was carried out after the segmentation of the data to avoid artifacts caused if this step was applied directly to the grey level data.

3. Quantification results and discussion

First, volume fractions of each phase and their corresponding connectivity across the analyzed volume were determined. The sur-

face area of interfacial planes between two phases as well as the lengths of the three-phase boundary lines were evaluated. Then, the effective thermal, electronic and ionic conductivities of the electrode and the tortuosity of the solid phases were estimated by numerically solving the diffusive transport equation. Most of this quantitative analysis was performed with laboratory-developed C programs on a personal computer [dual CPU Intel® Xeon® E5440 @ 2.83 GHz, 32 GB RAM].

3.1. Volume fraction

The volume fractions calculated from 3D data provided the following results: 41% for pores, 33% for 8YSZ and 26% for Ni. The solid volume fractions have been estimated to 44% Ni and 56% 8YSZ in the studied anode, which agreed well with the expected values (i.e., 40 vol.% Ni/60 vol.% 8YSZ). This result provided evidence of the good representativity of the analyzed volume.

3.2. Volumetric connectivity

In order to verify the connectivity of each phase, a laboratory-developed program based on a Hoshen–Kopelman algorithm was employed [28]. Voxel after voxel, the program verified the connectivity. The voxels that were linked together by a face were judged to be connected to form a cluster. When two voxels were only linked by a vertex or an edge, they were considered not to be connected.
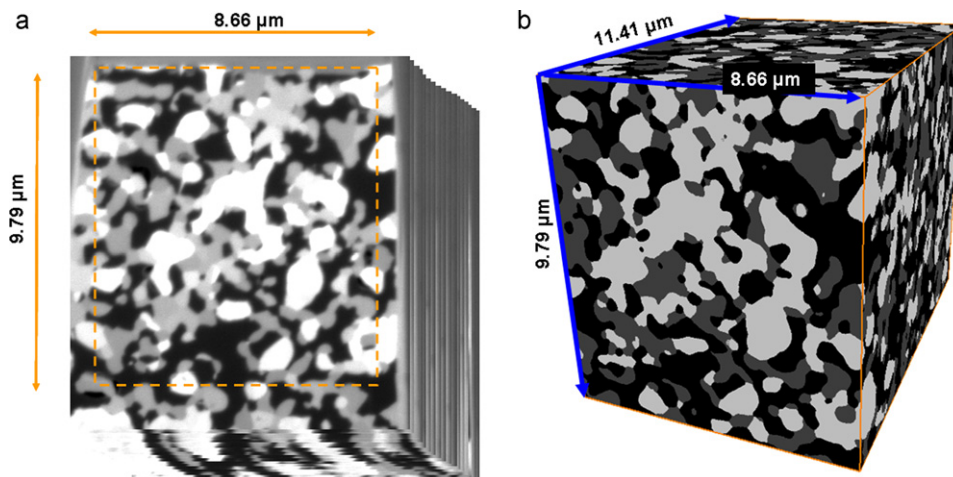

Fig. 4. Images of: (a) one of the original 115 serial-sections collected with a BSE detector, so that Ni appears brighter than 8YSZ and the impregnated pores appear dark, (b) final 3D image after alignment, delineating, cropping and adjustment of voxel size operations showing Ni (bright), 8YSZ (grey) and pore (dark) phases.
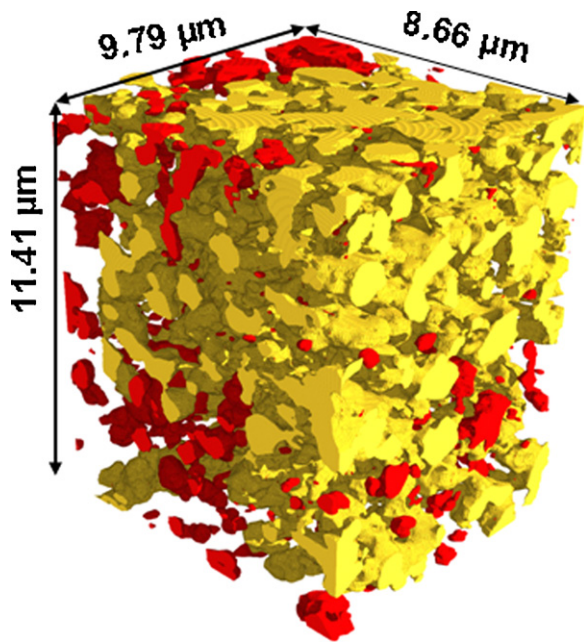
Fig. 5. An Ni cluster representation displaying that the main part (87.4%) of the Ni phase was percolated, i.e., in contact with the six boundary faces of the volume (in yellow).

Fig. 6. Pie diagram representing the specific surface areas of pores, 8YSZ and Ni, and the specific interface areas between the three neighboring phases (surface and interface are normalized by volume sample). The active TPB_L is 7.4 $\mu m\,\mu m^{-3}$.

This cluster neighborhood rule is commonly used in connectivity analysis [29]. Finally, if a cluster was connected to the six boundary faces of the studied volume, it was defined as "percolated", while others remained isolated (Fig. 5).

The performed analysis revealed that the three phases were mainly constituted of a very large "percolated" cluster which represented 99.8%, 99.1% and 87.4% of the pore, 8YSZ and Ni volumes, respectively. This significant percolation of all three phases suggested a good ability for the transport of gases in the pores, as well as of charge carriers in the solid phases.

3.3. Interface properties

Electrochemical and catalytic activities of an electrode are generally described by a single parameter: the TPB_L which is correlated to the number of regions where the electrochemical reactions can take place. However, the oxidation of the fuel involves numerous reaction steps which are not necessarily located at the TPB [20]. For example, adsorption and dissociation of hydrogen occur on the nickel surface because of its good catalytic properties. Thereby, only the Ni-pore interface, as opposed to the entire nickel surface, is exposed to the gas and can therefore react with the fuel. However, not all of the interfaces may be active due to non-contiguous regions (isolated cluster). Consequently, only the specific surface and interface areas inside the percolated volumes have been calculated, and the TPB_L was estimated for both the total and percolated volumes for comparison.

The specific surface areas (surface area normalized to the sample volume) were 4.27 $\mu m^2\,\mu m^{-3}$ and 4.24 $\mu m^2\,\mu m^{-3}$ for the porous and 8YSZ phases, respectively, and 2.33 $\mu m^2\,\mu m^{-3}$ for the Ni phase. The pie diagram of Fig. 6 indicates the specific interface areas (interface area normalized to the sample volume). For instance, the specific surface area of the Ni phase (2.33 $\mu m^2\,\mu m^{-3}$) was divided into Ni-pore (1.18 $\mu m^2\,\mu m^{-3}$) and Ni–8YSZ (1.15 $\mu m^2\,\mu m^{-3}$) interfaces. Thus, about 50% of the total nickel surface was exposed to the porous phase and could be used for surface catalytic reactions with the fuel.
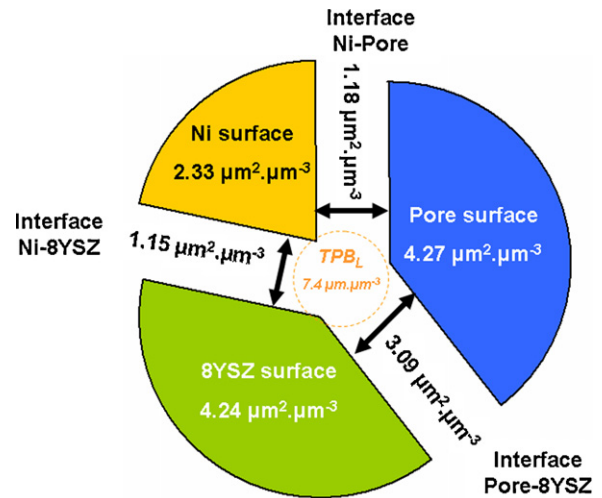
The TPBs are the regions where the three phases (pores, 8YSZ, Ni) met, thus corresponding – on the 3D image – to the edges of voxels common to the three phases [4]. A program has been developed to identify and count these edges. The following procedure was applied to each voxel by scanning the volume in the positive direction ($+x$, $+y$, $+z$), from the "first" voxel $(1,1,1)$ to the last one $(x_{max}, y_{max}, z_{max})$.

Considering the schematic representation of Fig. 7(a), if in the xy plane at least two of the three neighboring voxels have a nature differing from that of the studied voxel, the corresponding edge of contact between the three phases (designated edge 1 in Fig. 7(a)) is labeled a TPB. The same method was applied in the xz plane and yz planes, leading respectively to edge 2 and edge 3 (Fig. 7(a)). The TPB_L was calculated by summing edge 1, edge 2 and edge 3 all over the dataset, and this value was then normalized to the studied volume. By using this procedure, double counting of a TPB interface unit could be avoided [4].

This TPB analysis procedure was first applied to the initial volume and yielded a TPB density of 11.2 $\mu m\,\mu m^{-3}$. The 3D visualization of these TPBs was not easy since elementary voxels have to be represented into edges. Fig. 7(b) represents the voxels assigned to pores containing at least one TPB, because the graphic software does not support edge voxel representation. However, more than
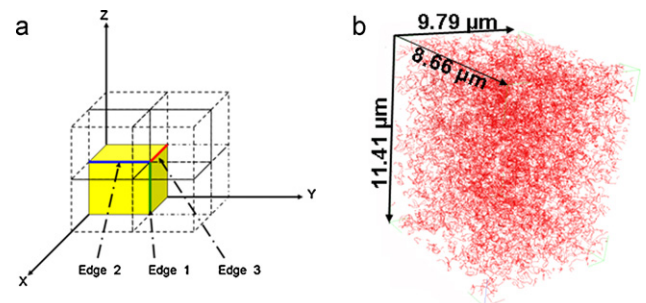

Fig. 7. (a) Determination of TPB_L from the edge segment length measurement: in the xy plane, if at least two of the three neighboring voxels correspond to a different phase than the considered voxel (in yellow), the corresponding edge of contact between the three phases (edge 1) is labeled as a TPB. The same method is applied in the xz plane and yz planes, giving edges 2 and 3, respectively. Finally, edges 1, 2 and 3 are summed and divided by the volume dimension to calculate TPB_L. (b) A 3D map of the "active" TPBs: all voxels assigned to pores and containing at least one active TPB are represented. (For interpretation of the references to color in this figure legend, the reader is referred to the web version of the article.)

one TPB can belong to a pore voxel and as a consequence it induces an under-representation of the total number of TPBs (statistically for 100 TPB edges, only 60 voxels are represented).

The "activity" of a TPB is subject to numerous definitions in the literature. A majority of authors have defined a TPB as "active" if it comprises three percolated phases (pore, Ni, 8YSZ) [4,6,8,10,11,16,17,20]. A TPB can also be defined as "active" if the three following conditions are verified: (1) there is a contiguous network of 8YSZ from the TPB of interest to the electrolyte, (2) there is a contiguous network of Ni from the TPB of interest to the current collector and (3) there is a contiguous network of pores from the TPB of interest to the inlet of the gas [30]. However, this last definition can only be used if the reconstructed volume is extended from the electrolyte to the collector.

The first definition was here applied to the TPB research procedure on the percolated volumes as mentioned before. The "active" TPB_L was calculated and found equal to 7.4 μm μm^{-3}, which represents 66% of the TPB_L calculated before and corresponding to the total volume. This value was relatively high compared to others reported in the literature (based on the same TPB_L calculation method) which were in the range: 2–10 μm μm^{-3} [6–8,15,16]. This suggests an elevated electrochemical performance for the studied electrode. The calculation of the 3D parameters: volume fraction, connectivity, and interface parameters were done simultaneously and completed in approximately 5 min.

It is worth noticing that certain mathematical corrections [11] or other TPB research approaches like the "centroid method" or the "voxel expansion method" [17,18] have been reported in the literature in order to take into account the "step-like" pattern of voxels edges, giving more accurate results. The main point is to compare tortuosity values evaluated by the same method.

3.4. Effective conductivities and tortuosity calculations

3.4.1. Definition of tortuosity

The term tortuosity is typically introduced as some kind of "fudge" factor in macroscopic transport equations to take into account the complex transport paths in a heterogeneous media. In a geometrical approach, the tortuosity (τ) is defined as the ratio of the "effective average path" (L_{eff}) of a fluid particle to the corresponding straight and shortest distance L along the direction of macroscopic flux [31]. Tortuosity is a parameter generally used to describe mass transport phenomena inside a porous phase, but it can also be extended to other transport processes including electronic, and ionic in the solid phases. Some attempts to measure this 3D parameter have already been made experimentally through a gas counter diffusion method [32] or saturation current density measurement [33]. However, the most reported procedure for estimating the tortuosity is based on the 3D analysis of a porous medium from X-ray or FIB tomography [4,6,34].

In most cases, tortuosity values can be deduced from a homogenization approach. In the case of a heterogeneous (real) material with anisotropic properties and geometrical complexity, the homogenization technique is an efficient method to obtain averaged properties equivalent to those of a homogeneous medium [35,36]. This methodology has been reported for numerical reconstructed composite electrodes (randomly distributed spherical particles) [6,37,38]. An alternative approach is to apply a Lattice Boltzmann Method (LBM) to solve a diffusion equation and calculate a phase tortuosity. Iwai et al. [17] compared a random-walk method with an LBM approach and similar tortuosity values were obtained. In the present work, the homogenization approach was used by solving the diffusive transport equation by means of a finite difference method [39].

Diffusion through a medium is usually described by Eq. (1):

$$\vec{J} = -D_0 \vec{\nabla}\theta \tag{1}$$

where $\vec{\nabla}\theta$ is the gradient of (i) the temperature in the case of heat conduction, (ii) the electronic potential in the case of electronic conduction, (iii) the ionic potential in the case of ionic conduction and (iv) the concentration in the case of mass diffusion, $\vec{J}$ is the flux of heat, electron, ions or gas and D_0 is (i) the thermal conductivity for heat conduction, (ii) the electronic conductivity for electron conduction, (iii) the ionic conductivity for ionic conduction transport and (iv) the diffusion coefficient for the mass diffusion.

In the case of a multiphase material, Eq. (1) was empirically corrected [31,34,40] by the diffusivity factor (Ψ) to take into account the presence of the phases in which the transport does not occur (for example, the solid phase in the case of the mass transport). Eq. (1) becomes:

$$\vec{J} = -D \vec{\nabla}\theta \tag{2}$$

where D is defined as the diffusion coefficient in the material with $D = \Psi D_0$. The diffusivity factor (Ψ) is linked to the tortuosity (τ) as follow [40]:

$$\Psi = \frac{\varepsilon}{\tau^2} \tag{3}$$

here, ε represents the phase fraction in which the diffusion takes place.

Since D_0 corresponds to the thermal conductivity, as well as the electronic conductivity, the ionic conductivity and the diffusion coefficient, its values can be obtained from the literature. To calculate D, as mentioned above, the homogenization approach was performed through the determination of an effective parameter D_{eff}, similar to D but for the equivalent homogeneous medium. In this approach, the ballistic behavior was neglected since the mean free path of the diffusing species was assumed smaller than the characteristic size of the diffusing medium.

3.4.2. Effective diffusion coefficient calculation

In the absence of external sources and in the case of steady-state conditions, the distribution of θ (for all conduction or diffusion phenomena) in the material is governed by the diffusive transport equation [39]:

$$\vec{\nabla} \cdot (-D \vec{\nabla}\theta) = 0 \tag{4}$$

This equation was first numerically solved using an implicit finite difference method [6,39] to obtain the distribution of temperature, potential (electronic and ionic) and concentration. The following boundary conditions were fixed: for $x_i = 0$, $\theta = \theta_1$ and for $x_i = x_{i\,max}$ $\theta = \theta_2$; where x_i corresponds to either x, y or z (along the volume axes, cf. Figs. 2 and 4(b) for the direction of axes) while $\vec{\nabla}\theta = \vec{0}$ on the other faces.

Once the θ distribution within the volume was obtained, the average conductive flux (Φ) over a cross-section of the surface area S normal to the flux (in the direction of the unit vector $\vec{n}$) could be calculated according to:

$$\Phi = \iint_S - D_{voxel} \vec{\nabla}\theta \cdot \vec{n} \, dS \tag{5}$$

where D_{voxel} is the diffusion coefficient characteristic of the phase (depending of the considered phenomenon: heat, electronic or ionic conduction and mass diffusion) present in the considered voxel (Table 2).

For the equivalent homogeneous material, the average conduction flux Φ can be written [39]:

$$\Phi = D_{eff} S \frac{\theta_1 - \theta_2}{x_{i\,max}} \tag{6}$$

Table 2
Thermal, ionic and electronic conductivities at 1123 K of the pores, 8YSZ and Ni [48–52].

	Pores	8YSZ	Ni
λ (W m^{-1} K^{-1})	(H$_2$) 0.48 [48]	2 [49]	50 [50]
σ ionic (10^{-3} S cm^{-1})	0	14 [51]	10^{-5} [52]
σ electronic (S cm^{-1})	0	10^{-6} [52]	10^4 [52]

Before calculating D_{eff} in the x_i direction, it is important to ensure that the solution has converged properly. In this aim, the value of Φ was evaluated on each slice (in the x_i direction) and a mismatch of 10^{-3} between the smallest and the largest Φ value was chosen as the convergence criteria.

Since the boundary conditions were identical for the equivalent homogeneous material and the real material, the fluxes Φ must be equal and combining Eqs. (5) and (6) gives D_{eff} in the x_i direction:

$$D_{eff} = \frac{x_{i\,max}}{S(\theta_1 - \theta_2)} \iint_S \left(-D_{voxel} \frac{\partial \theta}{\partial x_i} \right) dS \qquad (7)$$

In the studied anode, the typical characteristic size of pore, Ni and 8YSZ particles was in the micrometer range as approximated from the 3D images of Fig. 4(b). In the case of electron, ion and heat transport, the corresponding mean free path was smaller than 100 nm [41–43] and the bulk diffusion regime assumption could be validated. However, this assumption was no longer available for H$_2$ diffusion since the mean free path of H$_2$ molecules in a porous medium (l_{H_2}) is too large.

l_{H_2} can be approximated by the following expression [40]:

$$l_{H_2} = \frac{RT}{\sqrt{2}\pi d_{H_2}^2 N_a P} \qquad (8)$$

where N_a is Avogadro's number, R is the gas constant, T is the temperature, d_{H_2} is the diameter of the H$_2$ molecule and P is the pressure.

At an operating temperature of 1123 K and a pressure of 10^5 Pa, corresponding to the electrochemical test and by assuming that $d_{H_2} = 0.2$ nm, the mean free path of hydrogen molecules was close to $l_{H_2} = 900$ nm. This value is comparable to the characteristic size of the pores. Consequently, H$_2$ diffusion in the studied anode was affected by the Knudsen effect which takes into account collisions of gaseous molecules with the solid phases. In order to correctly estimate the tortuosity of the porous phase, it was necessary to use a model which included both bulk and Knudsen diffusion processes, like the Dusty gas model [44]. Consequently, only heat, ion and electron diffusive transports were calculated in this work. The results are given in Table 3 where the different values of D_{eff} are reported under the form of thermal, electronic and ionic effective conductivities. The entire calculation was completed in approximately 7 h.

The effective thermal conductivity appeared quite isotropic with a slightly lower value in the z direction, close to 4 W m^{-1} K^{-1}. This value was within the same order of magnitude as those generally reported for SOFC anodes [45–47]. As observed in Table 3, the effective electronic conductivity appeared to be anisotropic: the $\sigma_{electronic}$ value in the z direction was smaller than the ones in the x and y directions. This could be explained by either a dissimilar Ni

Table 3
Thermal, electronic, and ionic effective conductivities in the x, y and z directions from the calculation of D_{eff} at $T = 1123$ K.

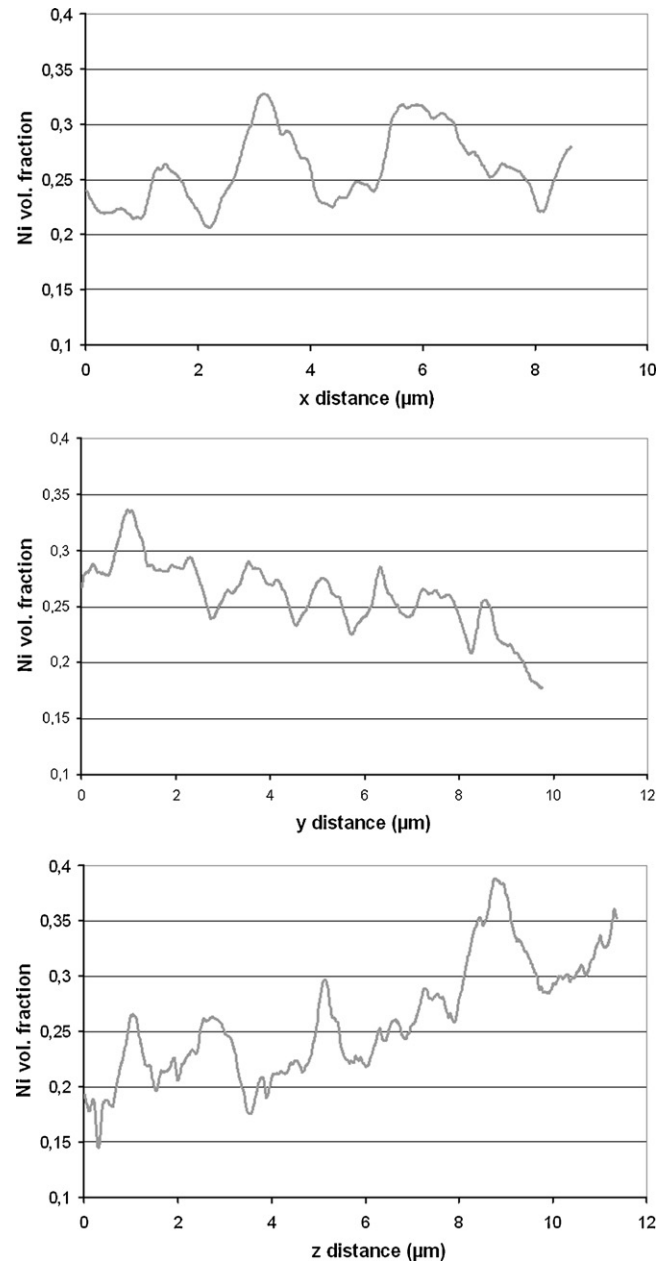|	x	y	z
λ (W m^{-1} K^{-1})	4.23	4.54	3.27
σ ionic (10^{-3} S cm^{-1})	1.43	1.19	1.03
σ electronic (S cm^{-1})	281	252	66

Fig. 8. The Ni volume ratio in the x, y and z directions of the studied volume.

concentration along the z direction as compared to along the x and y directions, or by a different distribution of Ni in the successive planes perpendicular to the z axis.

In the graph of Fig. 8, the Ni ratio in all the resampling planes is plotted in the three directions, showing few variations between them. As a consequence, the Ni distribution plays the most important role for the anisotropic electrical behavior. Experimental four-point electrical measurements performed at 1123 K on the anode surface led to a value equal to 81 S cm^{-1}. This value was within the same order of magnitude as its calculated counterparts and the difference between them can have many explanations, both from an experimental point of view and with regard to the signification of an average value compared to those given in the three directions.

The ionic conductivity in the studied anode was quite isotropic and close to 10^{-3} S cm^{-1}. Since a value of 1.4×10^{-2} S cm^{-1} had been used for the calculation, the microstructural effect for the loss

Table 4
Tortuosity of the 8YSZ and Ni phases in the x, y and z directions calculated by solving the transport equation by the finite difference method.

	x	y	z
τ_{8YSZ}	1.79	1.96	2.10
τ_{Ni}	3.04	3.18	6.24

of conductivity was near a factor 10. This factor might be different for another 8YSZ content and distribution inside the material.

3.4.3. Tortuosity results

As seen in Table 2, the ionic conductivity of Ni and pores, and the electronic conductivity of 8YSZ and pores were negligible. It was thus possible to deduce the tortuosity of the solid phases from the effective electrical and ionic conductivity values by combining Eqs. (1)–(3). Eqs. (9) and (10) allow the calculation of the tortuosity of the 8YSZ and Ni phases according to:

$$\tau_{8YSZ} = \sqrt{\varepsilon_{YSZ} \frac{D_{0(8YSZ)}}{D_{eff}}} \tag{9}$$

$$\tau_{Ni} = \sqrt{\varepsilon_{Ni} \frac{D_{0(Ni)}}{D_{eff}}} \tag{10}$$

where ε_{8YSZ} and ε_{Ni} are the 8YSZ and Ni volume fractions, respectively (cf. Section 3.1), D_0 (8YSZ) and D_0 (Ni) are the electrical and ionic conductivities of the 8YSZ and Ni phases (cf. Table 2). Moreover, τ_{8YSZ} and τ_{Ni} can be calculated in the x, y and z directions (see Table 4).

The tortuosity of the Ni phase, considered as the only electronic conductor, was higher in the z direction (6.24) as compared to in the x and y ones (3.04 and 3.18, respectively). This was not surprising since the value was directly deduced from D_{eff}. Using the same considerations, the tortuosity of the 8YSZ phase, considered as the only ionic conductor, gave more isotropic values as compared to other reported ones [12].

4. Conclusions

This work has focused on the 3D analysis of the microstructure in an Ni–8YSZ SOFC anode reconstructed by FIB tomography. Sample preparation, milling and imaging conditions as well as data processing have been optimized to obtain a high-quality representative 3D microstructure with the following dimensions: $8.66 \times 9.79 \times 11.41 \, \mu m^3$. Laboratory-developed programs rendered possible the calculation of some microstructural parameters such as the volume fraction, connectivity, specific surface and interface areas and TPB length including the proportion of active and non-active ones. These calculations demonstrated that for an anode with an initial 8YSZ/NiO volume ratio of 60/40, which after reduction gave volume relative amounts of 41% of pores, 33% of 8YSZ and 26% of Ni, all the phases were highly percolated. The active TPB length was estimated to $7.4 \, \mu m \, \mu m^{-3}$ which, in comparison to results reported in the literature, corresponds to an effective anode.

By solving the diffusive transport equation with finite difference calculations, the effective thermal, electronic and ionic conductivities could be determined. The tortuosity of the solid phases was deduced from these calculations. However, the tortuosity of the porous phase cannot be easily obtained from a "pure" diffusive mechanism due to the length of the mean free path of the fuel gas, which leads to Knudsen diffusion, is difficult to take into account. For this reason, as in the finite difference calculation presented in this paper, the tortuosity depends on the nature of the species that actually diffuse in the considered medium. No results have been given for the tortuosity of the porous phase. Some models are evaluated to eventually propose a simple geometrical description

of tortuosity able to provide an interesting comparison between materials with different Ni ratios, different sintering temperature, fabricated by different routes or after aging.

In a forthcoming paper, FIB tomography experiment and calculation procedures will be presented for Ni–8YSZ cermets of various compositions, ranging from 70/30 to 55/45 vol.% of 8YSZ/Ni. Microstructural parameters, interfacial features and tortuosity of the solid phases will be discussed as a function of the composition of the electrode.

References

[1] S. Singhal, K. Kendall, High-Temperature Solid Oxide Fuel Cells: Fundamentals Design and Applications, Elsevier Advanced Technology, Oxford, UK, 2003.
[2] P.R. Shearing, J. Gelb, N.P. Brandon, J. Eur. Ceram. Soc. 30 (2010) 1809–1814.
[3] P.R. Shearing, J. Gelb, J. Yi, W.-K. Lee, M. Drakopolous, N.P. Brandon, Electrochem. Commun. 12 (8) (2010) 1021–1024.
[4] K.N. Grew, A.A. Peracchio, A.S. Joshi, J.R. Izzo, W.K.S. Chiu, J. Power Sources 195 (24) (2010) 7930–7942.
[5] K.N. Grew, A.A. Peracchio, W.K.S. Chiu, J. Power Sources 195 (24) (2010) 7943–7958.
[6] J.R. Wilson, W. Kobsiriphat, R. Mendoza, H.-Y. Chen, J.M. Hiller, D.J. Miller, K. Thornton, P.W. Voorhees, S.B. Alder, S.A. Barnett, Nat. Mater. 5 (2006) 541–544.
[7] J.R. Wilson, S.A. Barnett, Electrochem. Solid-State Lett. 11 (10) (2008) B181–B185.
[8] J.R. Wilson, M. Gameiro, K. Mischaikow, W. Kalies, P.W. Voorhees, S.A. Barnett, Microsc. Microanal. 15 (2009) 71–77.
[9] S.A. Barnett, J.R. Wilson, W. Kobsiriphat, H.-Y. Chen, R. Mendoza, J.M. Hiller, D.J. Miller, K. Thornton, P.W. Voorhees, S.B. Alder, Microsc. Microanal. 13 (2007) 596–597.
[10] J.R. Wilson, A.T. Duong, M. Gameiro, H.-Y. Chen, D.R. Mumm, S.A. Barnett, Electrochem. Commun. 11 (2009) 1052–1056.
[11] J.R. Wilson, J.S. Cronin, A. Duong, S. Rukes, H-Yi. Chen, K. Thornton, D. Mumm, S. Barnett, J. Power Sources 195 (2010) 1829–1840.
[12] J.R. Wilson, J.S. Cronin, S.A. Barnett, Scr. Mater. (2010), doi:10.1016/j.scriptamat.2010.09.025.
[13] D. Gostovic, J.R. Smith, D.P. Kundinger, K.S. Jones, E.D. Washman, Electrochem. Solid-State Lett. 10 (12) (2007) B214–B217.
[14] J.R. Smith, A. Chen, D. Gostovic, D. Hickey, D. Kundiger, K.L. Duncan, R.T. DeHoff, K.S. Jones, E.D. Washman, Solid State Ionics 180 (2009) 90–98.
[15] P.R. Shearing, Q. Cai, J.I. Golbert, V. Yufit, C.S. Adjiman, N.P. Brandon, J. Power Sources 195 (15) (2010) 4804–4810.
[16] P.R. Shearing, J. Golbert, R.J. Chater, N.P. Brandon, Chem. Eng. Sci. 64 (2009) 3928–3933.
[17] H. Iwai, N. Shikazono, T. Matsui, H. Teshima, M. Kishimoto, R. Kishida, D. Hayashi, K. Matsuzaki, D. Kanno, M. Saito, H. Muroyama, K. Eguchi, N. Kasagi, H. Yoshida, J. Power Sources 195 (2010) 955–961.
[18] N. Shikazono, D. Kanno, K. Matsuzaki, H. Teshima, S. Sumino, N. Kasagi, J. Electrochem. Soc. 157 (5) (2010) B665–B672.
[19] P.S. Jorgensen, K.V. Hansen, R. Larsen, J.R. Bowen, Ultramicroscopy 110 (3) (2010) 216–228.
[20] L. Holzer, B. Munch, B. Iwanschitz, M. Cantoni, T. Hocker, Th. Graule, J. Power Sources (2010), doi:10.1016/j.powsour.2010.08.006.
[21] L. Holzer, B. Iwanschitz, T. Hocker, B. Munch, M. Prestat, D. Wiedemann, U. Vogt, P. Holtappels, J. Sfeir, A. Mai, T. Graule, J. Power Sources 196 (2011) 1279–1294.
[22] B. Ruger, J. Joos, A. Weber, T. Carraro, E. Ivers-Tiffée, ECS Trans. 25 (2) (2009) 1211–1220.
[23] L. Holzer, B. Muench, M. Wegmann, P.H. Gasser, R.J. Flatt, J. Am. Ceram. Soc. 89 (2006) 2577–2585.
[24] C.W. Tanner, K.Z. Fung, A.V. Virkar, J. Electrochem. Soc. 144 (1997) 21–30.
[25] K. Thyden, Y.L. Liu, J.B. Bilde-Sorensen, Solid State Ionics 178 (2008) 1984–1989.
[26] P. Hovington, D. Drouin, R. Gauvin, Scanning 19 (1997) 1–14.
[27] http://www.vsg3d.com.
[28] J. Hoshen, R. Kopelman, Phys. Rev. B. 1 (14) (1976) 3438–3445.
[29] Y. Nakashima, S. Kamiya, J. Nucl. Sci. Technol. 44 (9) (2007) 1233–1247.
[30] A. Abbaspour, N. Nandakumar, J. Luo, K.T. Chuang, J. Power Sources 161 (2006) 965–970.
[31] L. Shen, Z. Chen, Chem. Eng. Sci. 62 (2007) 3748–3755.
[32] R.E. Williford, L.A. Chick, G.D. Maupin, S.P. Simmer, J.W. Stevenson, J. Electrochem. Soc. 150 (8) (2003) A1067–A1072.
[33] C.L. Tsai, V.H. Schmidt, J. Power Sources 196 (2011) 692–699.
[34] A.S. Joshi, K.N. Grew, J.R. Izzo Jr., A.A. Perachio, W.K.S. Chiu, J. Fuel Cell Sci. Technol. 7 (2010) 011006.
[35] M. Kaminski, Int. J. Eng. Sci. 41 (2003) 1–29.
[36] Y.S. Song, J.R. Youn, Carbon 44 (2006) 710–717.
[37] J. Sanyal, G.M. Goldin, H. Zhu, R.J. Kee, J. Power Sources 195 (2010) 6671–6679.

[38] H.-W. Choi, A. Berson, B. Kenney, J.G. Pharoah, S. Beale, K. Karan, ECS Trans. 25 (2) (2009) 1341–1350.
[39] D. Rochais, G. Le Meur, V. Basini, G. Domingues, Nucl. Eng. Design 238 (2008) 3047–3059.
[40] T.G. Sherwood, R. L Pigford, C.R. Wilke, in: B.J. Clark, J.W. Maisel (Eds.), Mass Transfer, McGraw-Hill Inc., New York, 1975, pp. 39–43.
[41] S.P. Yuan, P.X. Jiang, Int. J. Thermophys. 27 (2) (2006) 581–595.
[42] J.M. Ziman, Electrons and Phonons, Oxford University Press, London, 1960.
[43] G. Soyez, J.A. Eastman, L.J. Thompson, G.R. Bai, P.M. Baldo, A.W. McCormick, Appl. Phys. Lett. 77 (8) (2000) 1155–1157.
[44] V.H. Schmidt, C.-L. Tsai, J. Power Sources 180 (2008) 253–264.
[45] M. Iwata, T. Hikosaka, M. Morita, T. Iwanari, K. Ito, K. Onda, Y. Esaki, Y. Sakaki, S. Nagata, Solid State Ionics 132 (2000) 297–308.
[46] H. Yakabe, T. Ogiwara, M. Hishinuma, I. Yasuda, J. Power Sources 102 (2001) 144–154.
[47] S. Kakaç, A. Pramuanjaroenkij, X.Y. Zhou, J. Hydrogen Energy 32 (2007) 761–786.
[48] D.R. Lide, Handbook of Chemistry and Physics, Thermal Conductivity of Gases, 89th ed, Taylor and Francis, Boca Raton, 2008, chap. 6 206.
[49] K.W. Schlichting, N.P. Padture, P.G. Klemens, J. Mater. Sci. 36 (2001) 3003–3010.
[50] Y.S. Touloukian, R.W. Powell, C.Y. Ho, P.G. Klemens, Thermophysical Properties of Matter. Thermal Conductivity, Metallic Elements and Alloys, vol. 1, IFI/Plenum, New York/Washington, 1970.
[51] R. Landauer, J. Appl. Phys. 23 (1952) 779–784.
[52] Z. Wu, M. Liu, Solid State Ionics 93 (1997) 65–84.